Experimental Investigation of the Effects of Aerospike Geometry on Aerodynamic Drag and Heat Transfer Rates for a Blunt Body Configuration at Hypersonic Mach Numbers

Srinath S[1] and Reddy K. P. J[2]
Department of Aerospace Engineering, Indian Institute of Science, Bangalore-560012, India

Abstract
The effects of aerospike geometry on the drag reduction and heat transfer rates for a large-angle blunt cone flying at hypersonic Mach numbers are investigated in a hypersonic shock tunnel. Two spike geometries are considered. The first is a plain spike with a conical tip and the second is a telescopic aerospike fitted with discs of decreasing diameter in the direction opposite to the flow direction. These aerospikes are fitted to a 120^o apex-angle blunt cone and results are investigated at free stream Mach numbers of 5.75 and 7.9 for different angles of attack. The aerodynamic forces are measured using an accelerometer-based force balance system and the heat transfer rates are measured using platinum thin film sensors. It is found that the telescopic aerospike has better drag reduction performance at angles of attack beyond 2^o while the performance of the plain aerospike is better for angles of attack closer to zero degrees.

NOMENCLATURE

a	= acceleration, m/s^2
C_d	= coefficient of Drag
h	= enthalpy, J/kg
M_∞	= free stream Mach number
M_s	= primary shock Mach number
P	= pressure, Pa
q	= heat transfer rate, W/cm^2
R_b	= base cone radius, mm
Re	= Reynolds Number, m^{-1}
r	= system response
s	= distance of Platinum thin film sensor from blunt cone nose, mm
St	= Stanton number
T	= temperature, K
V	= velocity, m/s
ρ	= density, kg/m^3

Subscripts

o	= total condition
∞	= free stream condition
w	= wall condition

[1]Research Student

[2]Professor, author for correspondence. Email: laser@aero.iisc.ernet.in

1. INTRODUCTION

The design of hypersonic flight vehicles is dominated by the issues of aerodynamic heating and aerodynamic drag. The problem of aerodynamic heating is mitigated by adopting a blunt nose configuration for vehicles flying at hypersonic Mach number. This has an associated effect of enhanced aerodynamic drag. The demand for hypersonic flight vehicles both for space travel and defense purposes has triggered global interest in the investigation of different drag reduction techniques for high drag configurations in recent times. The prominent techniques of drag reduction include the injection of a counter travelling cold jet [1, 2], the injection of a plasma jet against the freestream flow [3, 4], the addition of energy into the freestream flow and the addition of heat energy into the shock layer using exothermic reactions [5-7]. Large jet total pressures are required in the case of counter flow jet injection to produce jet-spikes in order to change the shock shape and to bring about a significant drag reduction. This spike flow is unsteady in nature and the thrust produced by such a spike flow results in a net increase in the overall drag, making the jet-spike counterproductive in practical situations. On the other hand, the technique of energy addition into the flow upstream of the vehicle, in general, results in enhanced heat transfer rate to the surface of the body. Both these techniques increase the complexity of the hypersonic vehicle system due to the addition of mechanisms for gas injection and energy addition in the flight.

A simplified and an effective alternative for reducing the aerodynamic drag and altering the heat transfer rates to the surface is to add a forward facing aerospike of appropriate dimensions in the nose region of the hypersonic flight vehicle. The aerospike could be expendable due to the severe heat loads during the ascent stage or detachable during the reentry stage where the aerobraking requires higher drag. The technique of drag reduction by use of an aerospike has been investigated widely. Zorea et al [8] reports an experimental study of the effect of spike length on the drag reduction at Mach numbers ranging from 1.5 to 2.25 at a freestream unit Reynolds number of $2x10^5$ (based on the length from the spike's tip apex to the tip shoulder). The results indicate that the maximum drag reduction is achieved when the spike length is equal to the base diameter of the blunt cone. Recently, Menezes et al. [9] investigated the effect of tip geometry of the aerospike on the percentage of drag reduction for large angle blunt cone in a hypersonic shock tunnel. The experimental measurements for a 120^o apex angle blunt cone at freestream Mach number of 5.75 show that an aerospike attached with a flat aerodisc at the tip yields an optimum drag reduction of about 50%.

While the plain aerospike is an effective means of substantial drag reduction, the technique suffers from the severe unsteady and oscillatory flows generated around the base of the aerospike leading to severe structural problems in practical applications. A proper understanding of spiked flows would give a better insight in modifying the spike configuration to overcome these problems. Crawford [10] investigated the flow over a spiked-cone hemisphere-cylinder configuration at a Mach number of 6.8. He analyzed the separation of the boundary layer with the variation of different unit Reynolds numbers ranging from $0.12x10^6$ to $1.5x10^6$ (based on diameters) and for different spike lengths. His investigations show that the separated boundary layer flow of the spiked body is similar to the flow boundary of a cone-cylinder. Maull [11] studied the flow over a blunt cone body with an aerospike at a flow Mach number of 6.8 and Reynolds number of $6.693x10^6$ /m. Based on this study, the author proposed the mechanism for the conical flow separation, re-attachment and flow oscillations. The boundary layer on the nose of the blunt body separates initially under the influence of the nearly normal shock wave of the body. If the spike protrudes through this shock wave, the separated layer will re-attach on the face of the body enclosing an approximately conical region. This region with circulatory flow is called the 'dead air region.' The conical shock wave which turns the main flow past this dead air region, is stronger and further influences the boundary layer for earlier separation. The interplay of scavenging the air from the dead air region, re-attachment of the flow and boundary layer interaction with an oblique shock results in the oscillation of the flow. Wood [12] investigated the factors which control the shape and size of the steady separated flow region in order to provide a basis for prediction of unsteady flow around blunt bodies with short spikes. He identified five different flow conditions on a blunt cone with a spike based on the cone angle. Rolf et al. [13] measured the fluctuating pressure

environment in the region of flow separation which is induced by a disc tipped spike at Mach numbers ranging from 0.6 to 3.5. They found that the maximum pressure fluctuations were because of the shock-shock interaction due to incipient reattachment of the disc wake on the spike at supersonic speed and therefore needs to be avoided to reduce the pressure fluctuations. Recently, Kobayashi et al. [14] proposed a new supersonic inlet device called a Multi-Row-Disc (MRD) with the disc and cavities formed over an 8^o cone to get a good pressure recovery. They also showed that the same device can be used as an aerospike for missile-shaped bodies to reduce the drag. They measured the drag and pressure recovery by varying the number of discs and with different cavities of length to depth ratio at Mach numbers ranging from 0.6 to 3. The pressure oscillations due to the cavities and the vibrations of the discs were also measured to monitor the resonance frequency. The results show that increasing the number of discs suppresses certain frequencies of flow oscillations and also improves the aerodynamic stability of the missiles. Based on these findings they propose this multi-row-disc (MRD) device with suitable modifications to reduce the drag for the blunt cone body.

In this paper we report the experimental investigations of the effects of aerospike geometry on the aerodynamic drag and heat transfer rates to the surface of a 120^o apex angle blunt cone in hypersonic flows at freestream Mach numbers of 5.75 and 7.9 at angles of attack varying from 0 to 10 degrees in the hypersonic shock tunnel HST2. The aerodynamic forces are measured using an accelerometer-based force balance system and the heat transfer rates are measured using platinum thin film sensors. Experimental data for the blunt cone model without an aerospike, the blunt cone with a conical tipped plain aerospike and the blunt cone with a telescopic aerospike are presented in graphical form for different angles of attack.

2. EXPERIMENTAL FACILITY AND MODEL DESCRIPTION

The experimental investigations were carried out in the hypersonic shock tunnel HST2 which consists of a 50 mm internal diameter shock tube divided into a 2.4 m long driver and a 6.0 m long driven section separated by an aluminium diaphragm. The end of the driven section is connected to a converging-diverging nozzle of 300 mm exit diameter with a detachable throat through a thin paper diaphragm. The exit of the conical nozzle is connected to a 450 mm long rectangular test section of 300 x 300 mm cross section which is attached to a dump tank-vacuum pump assembly. The flow Mach number of 5.75 is achieved in straight through mode while the Mach 7.9 flow is achieved by operating the tunnel in the reflected mode. In all the tests air is used as the test gas and helium as the driver gas. The flow enthalpy in the tunnel can be varied from 0.7 to 4.5 MJ/kg by using metallic diaphragms of different thicknesses. The typical test conditions obtained in HST2 are given in the Table.1.

Table 1. Test conditions

	For M_∞ =5.75	*For M_∞ = 7.9*
Driver gas	Helium	Helium
Driven gas	Air @ 150 mm of Hg	Air @ 150 mm of Hg
Primary Shock Mach number (M_S)	3.4	3.75
Total Pressure (P_o)	823 kN/m^2	1984 kN/m^2
Total temperature (T_o)	1796 K	2121 K
Total Enthalpy (H_o)	1.8 MJ/kg	2.13 MJ/Kg
Free stream pressure (P_∞)	0.515 kN/m^2	0.217 kN/m^2
Free stream temperature (T_∞)	218 K	156 K
Free stream density (ρ_∞)	0.00822 kg/m^3	0.0049 kg/m^3
Free stream velocity (V_∞)	1702 m/s	1980 m/s
Free stream Reynolds number (Re_∞)	0.978x10^6 /m	0.948x10^6 /m

The 120^o apex angle blunt cone test model consists of a spherical nose of radius 27 mm and conical frustum of 101 mm base diameter. The drag of this body can be theoretically estimated using modified

Newtonian theory [15] with the centrifugal force effect considered at the nose portion. The details of the blunt cone model are shown in Fig. 1. The nose tip was fitted with a metallic insert with 3-mm internal threads to fix the aerospike. The effective spike length of 100 mm was selected such that the ratio of the spike length to the model base diameter is 1 [8]. Two types of spikes were designed in which one was a plain aerospike with sharp conical tip of 10º cone angle and another one was the telescopic aerospike designed from a 10º cone with cavities formed over it. The cone angle of 10º was chosen to ensure that the aerodynamic body would be completely under the shadow of the conical shock wave emanating from the tip of the aerospike. The aerospike resembles that several disks of 2 mm thickness were attached to the above said plain spike with conical cavities of length equal to their mean depth. The blunt cone base was internally threaded to attach a 100-mm long hollow skirt which houses the force balance system. The blunt cone surface was flush mounted with two Macor pieces, each having six Platinum thin film heat transfer sensors deposited on them.

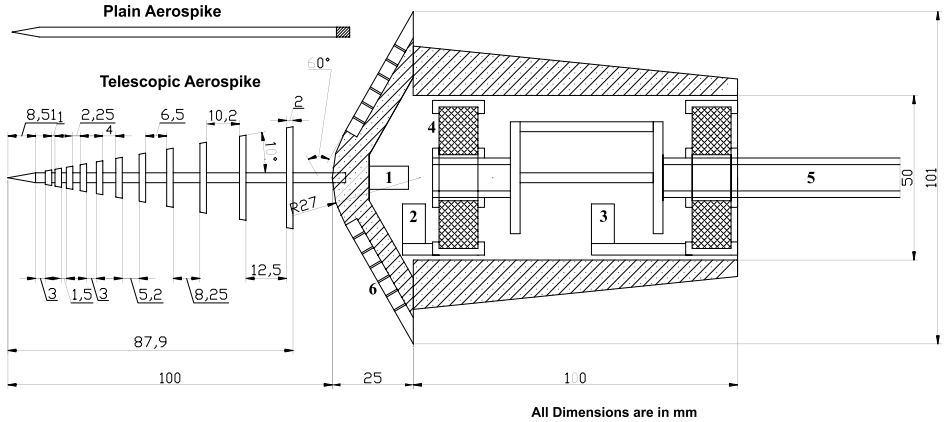

Figure 1. Schematic diagram of the blunt cone model (1, 2 and 3, - Drag, Front lift and Aft-lift accelerometers respectively; 4. Rubber bush; 5. Fastening sting; 6. Platinum thin film gauges).

3. VISUALIZATION OF HYPERSONIC FLOW OVER THE AERODYNAMIC MODEL

Flow visualization was done using the schlieren arrangement shown in Fig. 2 to understand the flow field around the models with and without an aerospike and the physical reasons for the effects of the aerospikes on the aerodynamic drag and heat transfer rates. The visualization experiments were carried out at different angles of attack for the freestream Mach number of 5.75 using a high speed camera (Phantom V7.1) capable of capturing 0.2 million frames per second. The schlieren pictures clearly show the details of the flow establishment and the shock interaction over the blunt cone surface.

The time sequence of the flow over the blunt cone body is shown in Fig. 3. These pictures show the development of a steady bow shock pattern in front of the blunt cone body without a spike from the initial starting of hypersonic flow. A similar time sequence of the flow patterns over the blunt cone with the telescopic spike at zero degrees angle of attack is shown in Fig. 4. Even though the model was mounted at zero degrees angle of attack, the schlieren images clearly indicate slight misalignment of the model with respect to the flow direction. It is seen that the oblique shock generated by the telescopic aerospike has encompassed an oscillating conical flow region and this buzzing phenomenon is due to the following sequential occurrences in the flow. If the flow beyond 1000 µs of time, which includes all the starting processes, is considered as steady state, the oblique shock assumes initially an asymptotic profile. Pressure in the conical flow region gets enhanced due to the complex flow phenomenon within the cavities created by the parallel disks of the spike causing the shock profile to bulge and, when the enhanced pressure exceeds the limit, the fluid is swept away through the gap between the blunt body periphery and the shock profile. Once the fluid is swept away again the oblique

shock forms an asymptotic profile. Moreover this shock disperses as it extends along the flow to accommodate the fluid particles state to the adjacent flow streamlines. The schematic representation of the flow pattern for the blunt cone with telescopic spike is presented in Fig. 5. The conical cavities formed over the spike generate shear layers at the edge of the discs. Since the conical cavities have a mean length-to-depth ratio of unity, these are considered as deep conical cavities which create a recirculation region [16]-[20]. Reattachment shock and expansion waves are generated when the flow seeps out from the blunt cone periphery.

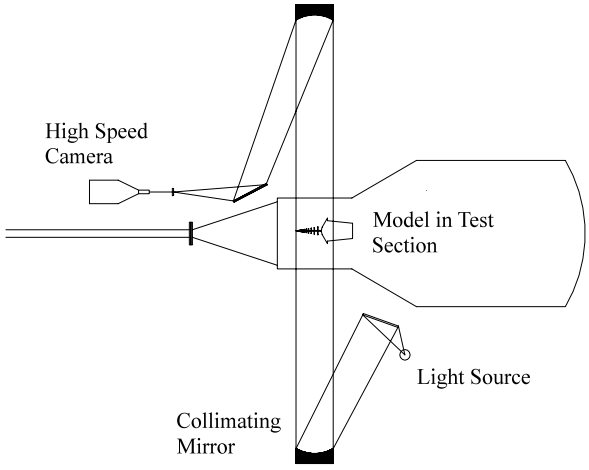

Figure 2. Z-type schlieren arrangement.

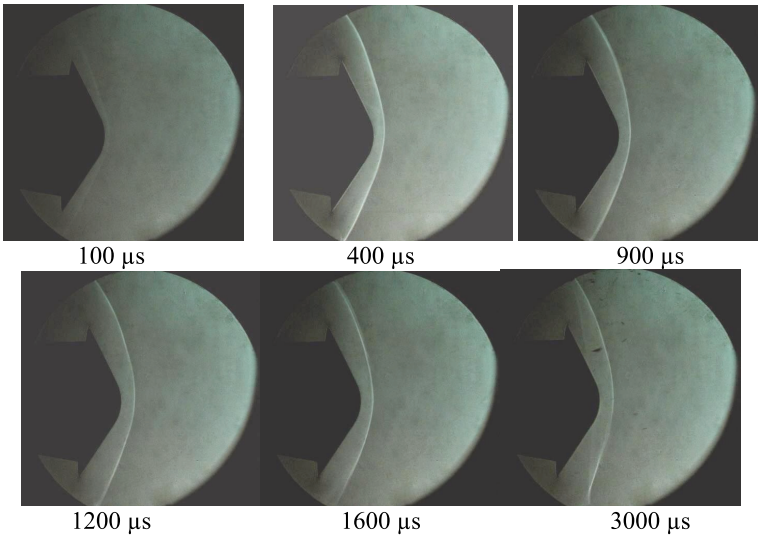

Figure 3. Schlieren pictures for the blunt cone without spike at Mach 5.75.

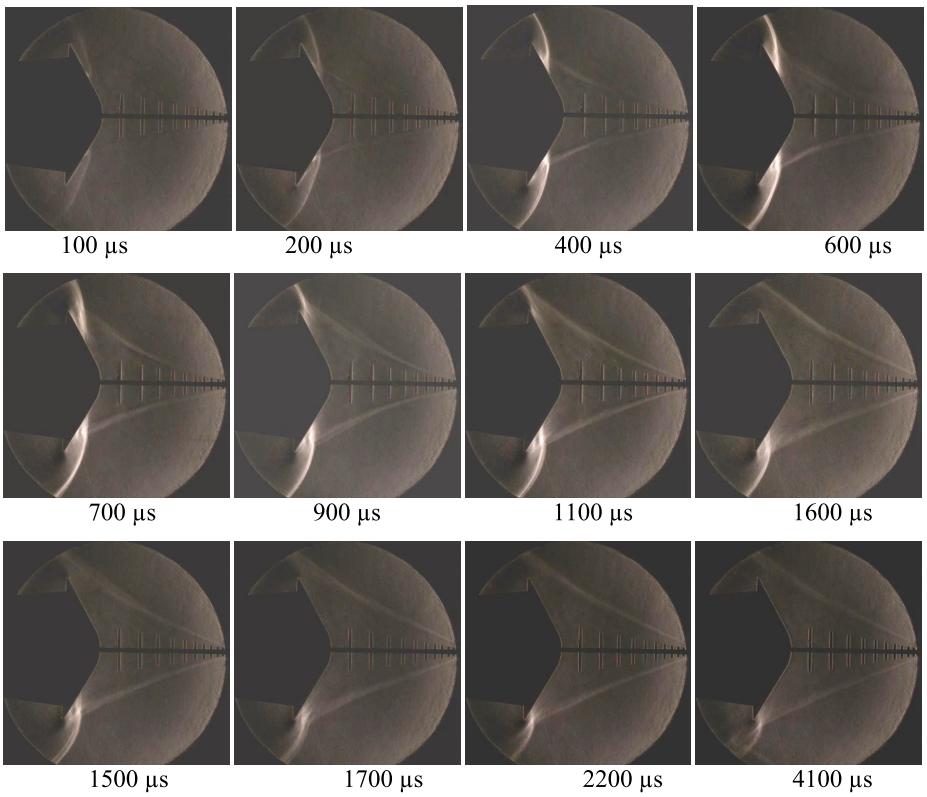

Figure 4. Schlieren pictures for blunt cone model with telescopsic spike at Mach 5.75.

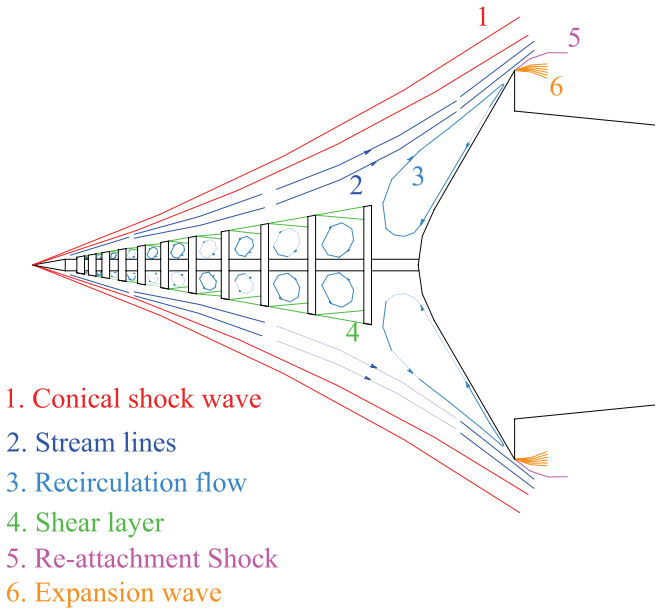

Figure 5. Schematic representation of proposed flow patterns around the blunt cone model with telescopic spike at zero degrees angle of attack in hypersonic flow.

The schlieren pictures shown in Figs. 6-8 show the time histories of the flow for the model at 2º, 6º and 8º angles of attack, respectively. As the angle of attack increases the flow oscillations reduce and there is an interaction between the oblique shock and the re-attachment shock over the windward side of the blunt cone surface. This shock interaction comes closer towards the blunt cone nose when the angle of attack increases. At and beyond 6º angle of attack there are multiple shocks in the windward side generated from each and every disk with variation in angles as the flow passes through every shock and they collide to form a single primary shock and this interacts with the re-attachment shock over the blunt cone body. In the leeward side a re-attachment shock is visible and this is due to the flow getting accelerated to supersonic speeds. For angles of attack less than 6º, this re-attachment shock is not observed in the leeward side. Also, on the leeward side, the oblique shock faces a sudden deflection in its angle. This may be due to the supersonic flow in this region. Fig. 9 shows the schematic representation of multi shock profiles at 8º angle of attack.

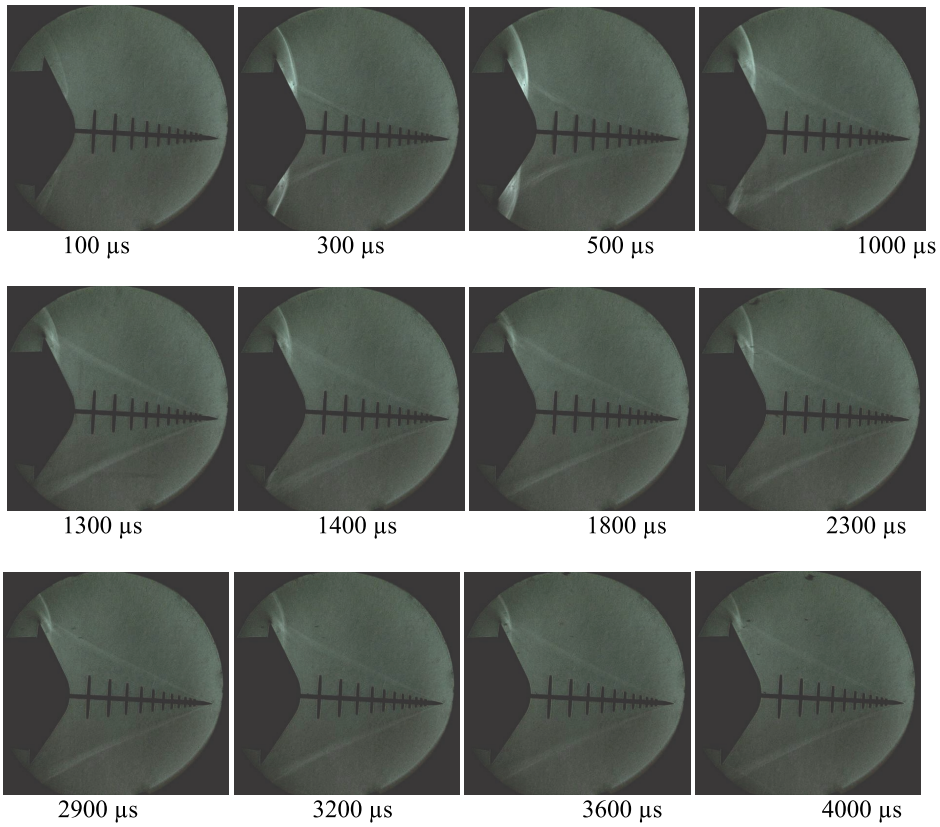

Figure 6. Time history of flow at 2º angle of attack at Mach 5.75.

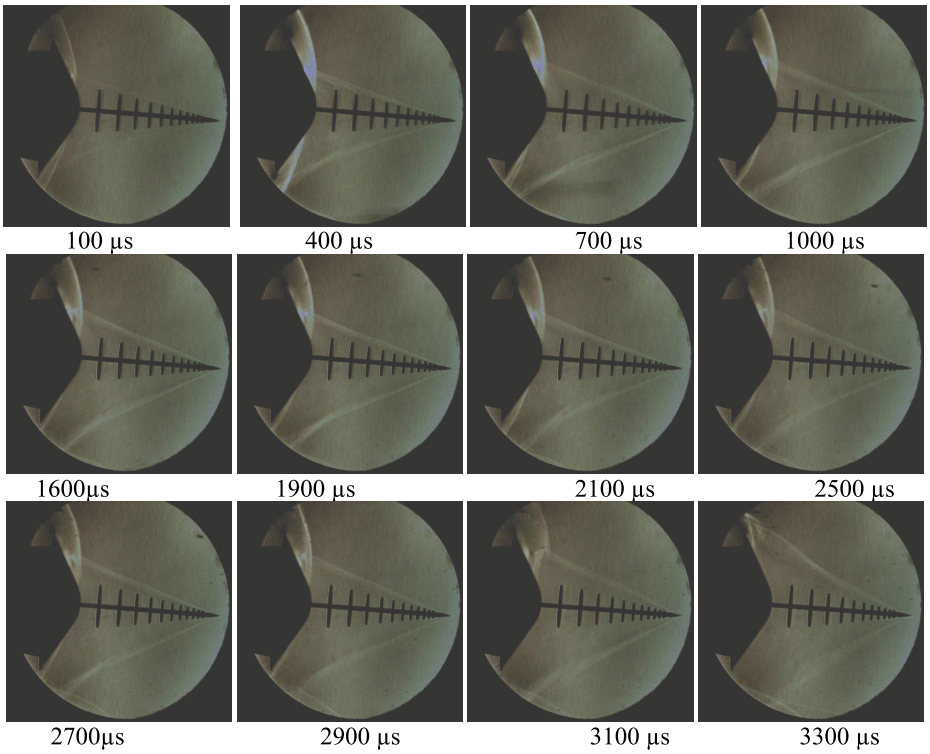

Figure 7. Time history of flow at 6° angle of attack at Mach 5.75.

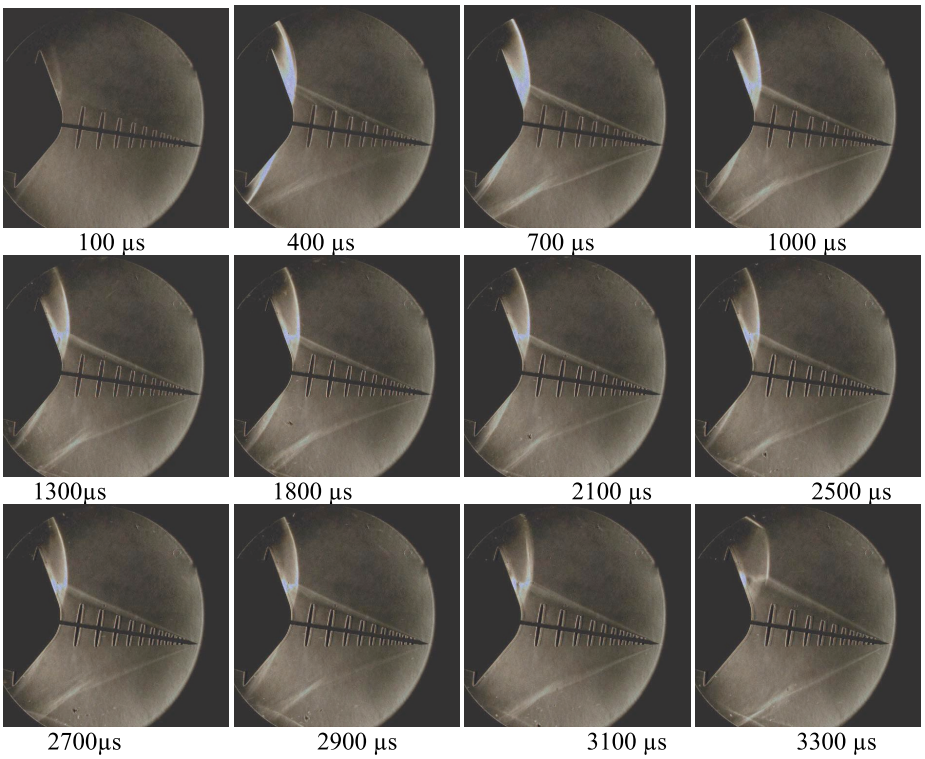

Figure 8. Time history of flow at 8° angle of attack at Mach 5.75.

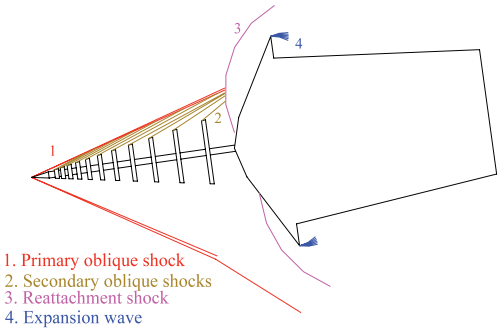

Figure 9. Schematic representation of the proposed flow pattern around the blunt cone model with telescopic spike at angle of attack in hypersonic flow.

4. MEASUREMENT OF DRAG AND HEAT TRANSFER RATES

The drag measurements for the blunt cone body without a spike, with the conical tipped plain spike and with the telescopic spike were performed using the three component accelerometer based force balance system which is capable of measuring the drag, lift and pitching moment of the body [21]. However, since we are interested in the drag reduction studies we present the results of only the drag measurements in this paper. Primarily the drag force measurement was done based on Newton's second law of motion by measuring the acceleration of the aerodynamic model in the hypersonic flow. The details of the balance system are given in the schematic diagram shown in Fig. 10. The existing design, used by Menezes et al. [9], was modified with a 2-mm grove on the inner side of the steel rings and at the fastening sting as a protective covering for the rubber bushes. This enhanced the life of the rubber bushes substantially. The total design of the aerodynamic model was based on the location of center of gravity between rubber bushes to avoid any drooping. The force balance system was attached to the skirt portion of the model using screws through the steel rings. This enables the model to move as a free body due to the negligible resistance from the rubber bushes during the hypersonic flow. The drag, front lift and aft lift accelerometers in the force balance system were connected to a PC based data acquisition system to store the analog signals in digital format. The actual drag signal was obtained from the raw signals by deconvoluting with the system response function derived from the calibration procedure of the force balance system using a hammer.

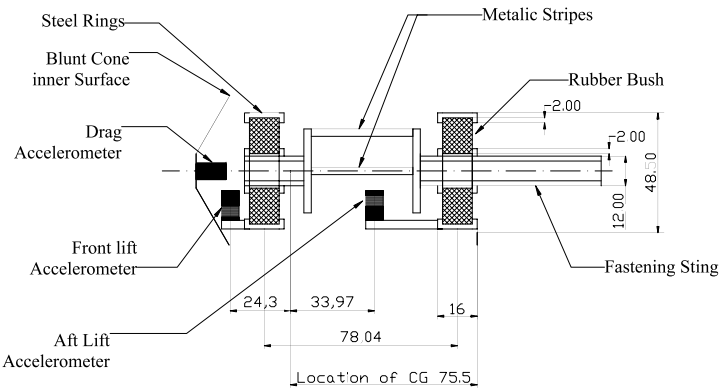

Figure 10. Schematic diagram of the accelerometer-based force balance system

When there is hypersonic flow of about a millisecond duration in the test section of the shock tunnel, the aerodynamic body is subjected to an impulse loading. The body in the test section accelerates due to its

free floating conditions ensured by the negligible resistance offered by the rubber bushes during the short run time of the tunnel [22, 23]. The acceleration of the body was measured using M/s PCB piezotronic accelerometers with 100 mV/g sensitivity. A typical drag accelerometer signal is shown in Fig. 11.

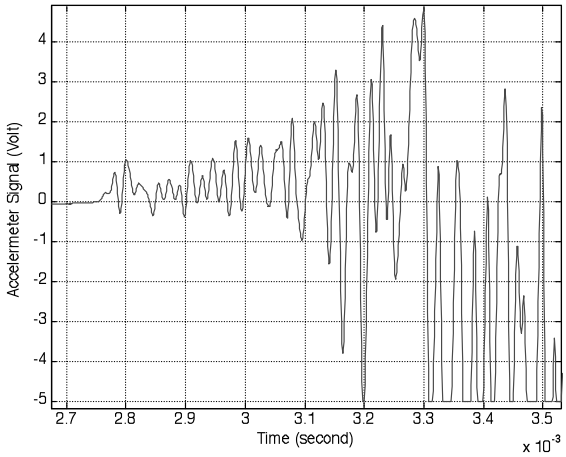

Figure 11. Typical drag accelerometer signal for telescopic spiked blunt cone body.

A mathematical expression for the convolution of the force balance system response r(t) with the force f(t) giving the output acceleration a(t) is as follows.

$$a(t) = \int_{-\infty}^{+\infty} f(t) r(t-\tau) d\tau \tag{1}$$

Deconvolution is the process of recovering input f(t) from the output signal a(t). In the frequency domain the deconvolution is represented by

$$F(f) = \frac{A(f)}{R(f)} \tag{2}$$

where R(f) is the transfer function of the force balance system. Identifying this transfer function is essential to adopt the proper deconvolution methodology. This was done by calibrating the force balance system in which the response of the force balance system was found by giving a known impulse input and recording the corresponding output of the accelerometer. The impulse force was given along the axis of the blunt cone model at its nose tip by a standard impulse hammer with the sensitivity of 12.65 mV/N (M/s PCB Piezotronics). The impulse signal and the corresponding accelerometer signals were stored in a PC through a data acquisition system. These signals give a better understanding of kinetics of the body. Fig. 12 shows typical calibration signals which show that once the impulse is given to the body, the drag accelerometer senses initially a positive jerk (time rate of change of acceleration) then attains a maximum acceleration and then a negative jerk until there is an increase in the impulse force. When the impulse force reduces the body starts moving in the reverse direction which is seen from the increase after the negative jerk in the accelerometer signal. Therefore, approximately only the initial 360 microseconds is considered as the useful calibration signal and is used for the deconvolution process. In the second step of the calibration, the signals are subjected to the deconvolution of original input impulse signal from the recorded output calibration signal by using the method of discrete constrained iterative deconvolution technique as described below.

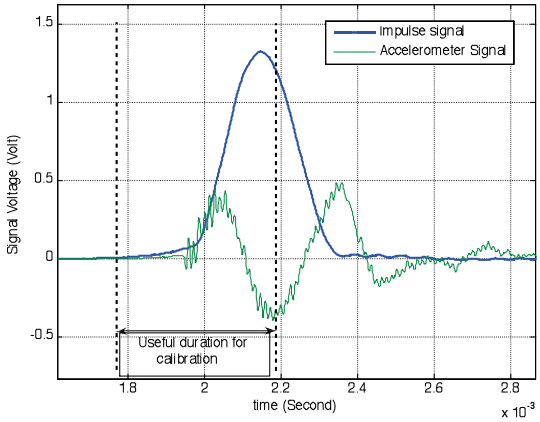

Figure 12. Calibration signals

Prost and Goutte [24] developed three discrete constrained iterative deconvolution algorithms in which the extended conjugate gradient algorithm has the optimized convergence rate and this method is adopted for doing the deconvolution of the drag accelerometer signals. Although the force balance system is a non-linear system, we assume that it is a linear and shift-invariant system for short times to adopt this technique. Therefore this deconvolution technique is capable of restoring the signal for the initial 500 to 600 microseconds of the millisecond test time. The flow chart of the discrete conjugate gradient algorithm is given in Fig. 13, where $\hat{A}$ is the experimental accelerometer signal,$\hat{C}$ is the cascaded matrix operator, $\hat{R}$ is the system response, $\hat{D}(n)$ is the recovered drag input after the nth iteration, $\hat{E}_c(n)$ is the nth iteration error, $\hat{H}$ is the Toeplitz matrix of the system response and n is the number of iterations.

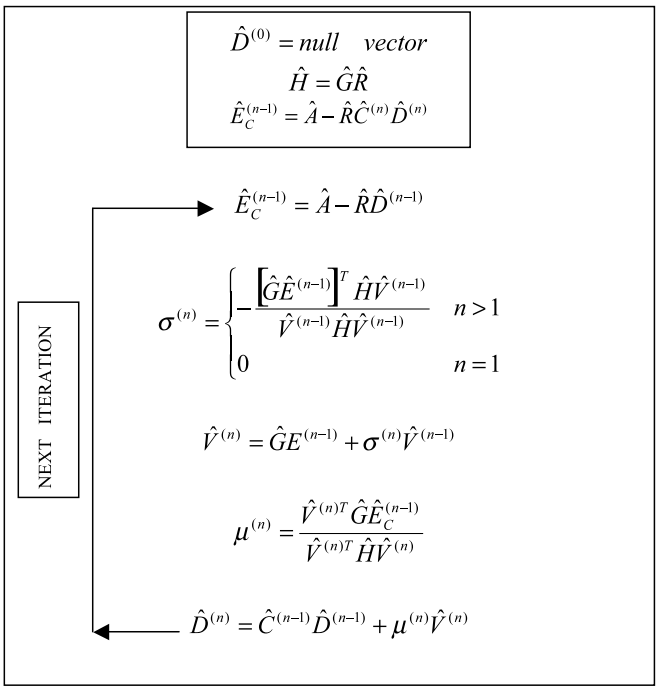

Figure 13. Flow chart of discrete conjugate gradient algorithm.

A Matlab Program was written based on this deconvolution technique. Initially the calibration signal from the impulse hammer was recovered from the recorded output signal as a test case. Fig. 14 shows the comparison of the input impulse hammer signal with the recovered signal after deconvolution of the accelerometer output. In the process of deconvolution at the end of every iteration, high frequency noises were getting added with the resultant of the deconvolution. To eliminate this noise a low pass filter was used. The cut off frequency of this low-pass filter cannot be selected in every iteration and therefore an optimized value was selected based on a trial and error method, such that the base signal does not get affected. The number of iterations for the deconvolution of the raw accelerometer signal primarily depends upon the number of samples selected which decides the frequency spectrum for processing, size of the window and the cut off frequency of the low-pass filter.

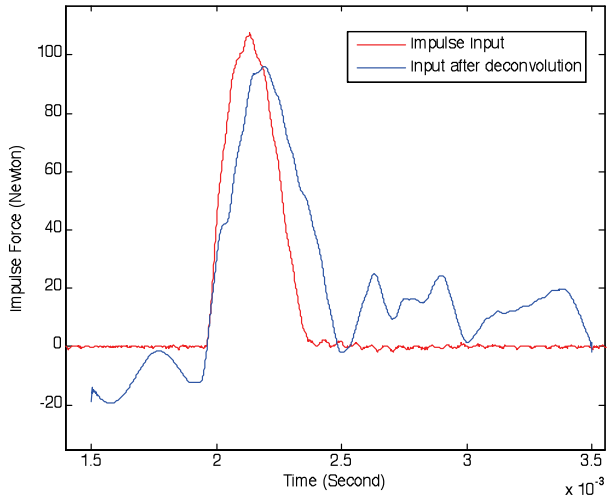

Figure 14. Recovered calibration signal after deconvolution compared with the impulse signal.

The heat transfer rates were measured using Platinum thin film sensors formed over a thermally insulating backing material of Macor. They were flush mounted into the test model surface. In the present case two slots were formed on either side of the nose tip over the blunt cone surface and on each side six platinum thin film gauges were formed on the Macor inserts by vacuum deposition using a sputtering technique. Figure 15 shows a picture of the blunt cone model with the Platinum thin film gauges.

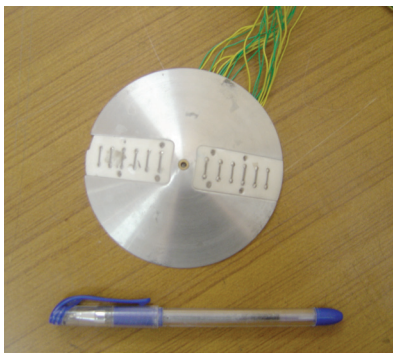

Figure 15. Blunt cone model with the Platinum thin film gauges formed on Macor substrate.

The passive platinum thin film sensor was provided with an initial power supply depending upon the resistance to maintain a constant current of 20 mA. The gauges had resistances ranging from 12 to 18 ohms initially. The heat transfer rates were derived from the recorded time history of the temperature sensed by these platinum thin film gauges using a numerical procedure given by Cook [25].

5. RESULTS AND DISCUSSION

The experiments were carried out for the model without any spike, with the plain spike and with the telescopic spike at different angles of attack ranging from 0 to 10 degree at 2 degree intervals. Raw signals from the drag accelerometer are shown in Fig. 16 for the three cases. The recovered signals after deconvolution are shown in Fig. 17 for zero degree angle of attack. It was seen that this deconvolution process recovers the drag signal only for the initial 500 to 600 microseconds of the total test time. The behavior of the force balance system becomes non-linear after this time probably due to the reaction of the rubber bushes. The number of iterations needed for the deconvolution was in the order of several thousand, which is time consuming. Therefore a better deconvolution methodology needs to be found and adopted.

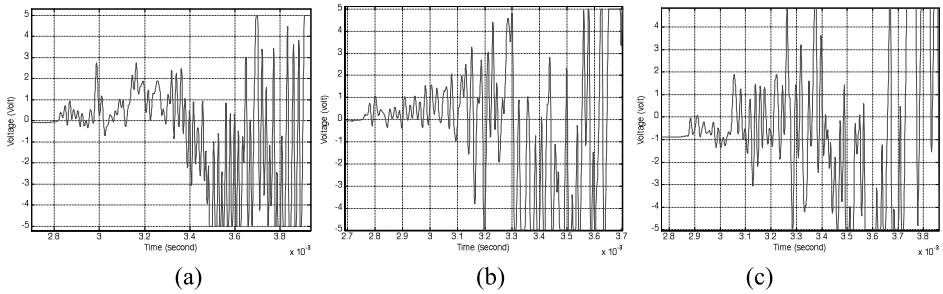

Figure 16. Raw accelerometer signals for (a). Model without spike, (b) Model with plain spike and (c) Model with telescopic spike.

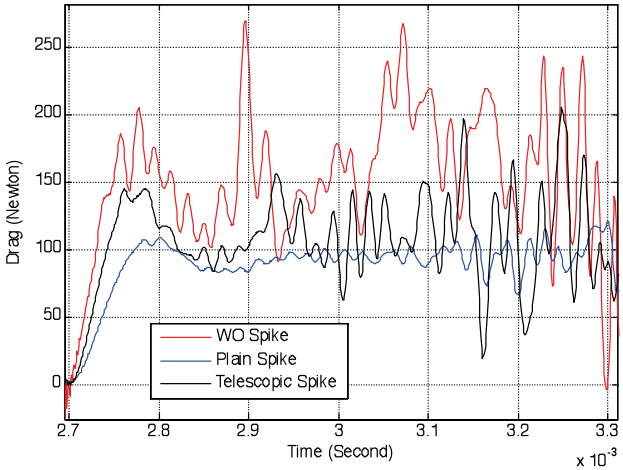

Figure 17. Recovered signals after deconvolution at Mach 7.9.

The drag accelerometer signals gave an understanding of the dynamics of the model during the flow. Compared to the signal from the model without any spike, the signal from the model with a spike has high frequency content which may be due to the flow instabilities induced by the spike. After the deconvolution of the drag history it is seen that about 400 microseconds of constant axial force is felt by the model during the steady hypersonic flow.

In general, total drag of the aerodynamic body is the sum of components of axial and normal forces which are found from the respective accelerometer signals.

$$D = F_A \times \cos(\alpha) + F_N \times \sin(\alpha)$$

Where F_A and F_N are axial and normal forces respectively. In the calculation of the coefficient of drag, only the axial force was considered and found as follows

$$C_d = \frac{F_A \times \cos(\alpha)}{0.5\rho_\infty A V_\infty^2}$$

The measured values of the drag coefficient are compared with the estimated values using modified Newtonian theory in Fig. 18 for different angles of attack. The error in C_d was estimated to be within 5.37% based on the uncertainty analysis of the measurement system. The drag of the spiked blunt body depends on the separated flow region and also the shock interaction over the blunt cone surface. From the results it is found that the drag is greatly reduced by using the spikes. At zero angle of attack it is seen that the introduction of the plain spike and the telescopic spike reduced the drag coefficient by 38% and 29%, respectively. At a 2º angle of attack the drag for the body with the telescopic spike increases compared to that for the body without any spike because of addition of the stabilizer disks and also because the shock impinges on the body surface. Beyond 2º angle of attack, the shock interaction over the blunt body surface slips out in the leeward side while on the windward side the shock interaction comes closer towards the nose. Therefore, the flow separation created by the stabilizer disk is high which results in the decrease of pressure on the blunt cone surface. The drag reduction for the telescopic spike configuration is due to this slipping out of the shock interaction over the surface and the low pressure region at the leeward side. But in the case of the plain spike the flow separation is not that large and therefore the drag increases when compared to the configuration without a spike at 4º angle of attack and beyond. At 6º angle of attack, the maximum drag reduction of 54% is observed for the telescopic spike. Hence it is found that the telescopic spike is a better drag reduction device than the conical tipped plain spike for the blunt cone body at higher angles of attack. Figure19 shows the percentage of drag reduction due to the spikes when compared to that measured for the blunt cone body without a spike.

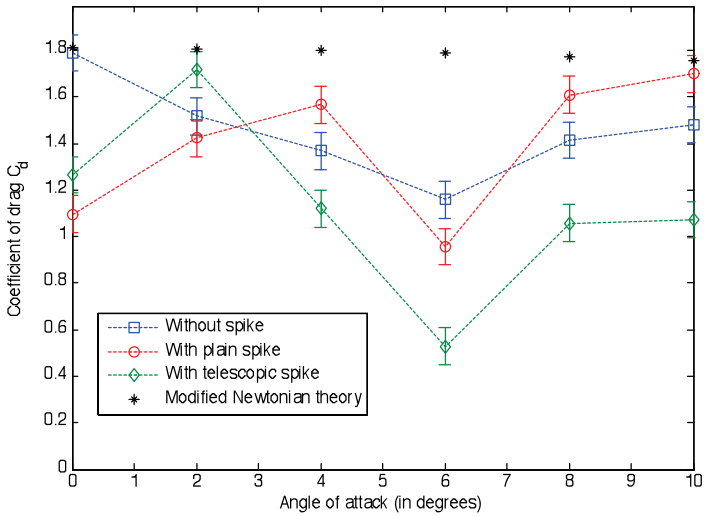

Figure 18. Comparison of the measured and estimated drag values for different angles of attack at Mach 7.9.

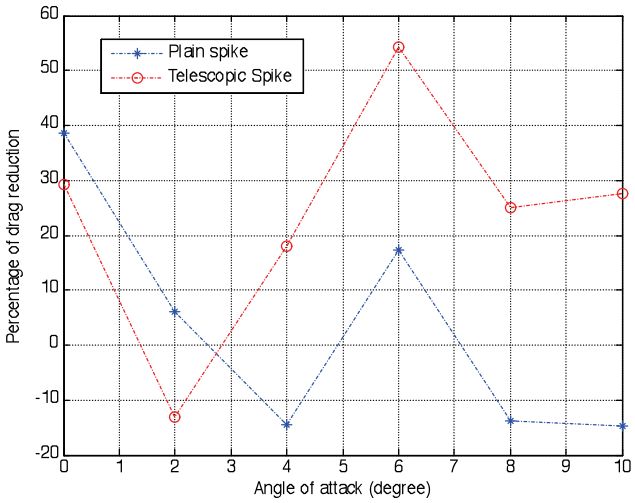

Figure 19. Comparison of percentage of drag reduction for blunt cone body with plain and telescopic aerospikes.

Hypersonic flow over a blunt body creates a shock layer, having large thermal energy, which results in high heating rates of the aerodynamic vehicle, particularly in the stagnation point of the flow over the body. But when the blunt cone body is attached with a forward facing spike protruding from the nose tip, it would change the bow shock pattern into conical shock pattern leaving the blunt cone surface engulfed with a low energy re-circulation region resulting in reduced heating of the fore body. But the conical shock pattern interacts with the re-attachment shock over the blunt cone surface and this shock-shock interaction enhances the heating of the surface to levels higher than the stagnation point heating near the interaction point on the blunt body. In the present experimental studies, heat transfer rates over the blunt cone surface were measured for all the three cases of without any spike, with the conical tipped plain spike and the telescopic spike for angles of attack varying from 0 to 10 degree in steps of 2 at freestream flow Mach numbers of 5.75 and 7.9.

The first set of experiments was conducted for the models without any aerospike and with the telescopic aerospike at a free stream Mach number of 5.75 at angles of attack varying from 0 to 8 degrees in steps of 2 degrees with the model aligned in such a way that the thin film sensors were axi-symmetrical to the flow. Typical experimental heat transfer signals along the surface of the blunt cone without any aerospike starting from the stagnation point are shown in Fig. 20. Similarly, Fig. 21 shows the signals for the model with the conical tipped telescopic aerospike. The signals show that at s/R_b of 0.52 and 0.65 there is a large jump in voltage which corresponds to a temperature rise due to the shock-shock interaction at these points. At s/R_b = 0.52 the output signal voltage variation is smaller than that for the blunt cone without any spike and also it does not show a parabolic rise. This is due to the presence of the disc close to the base of the spike which blocks the heat transfer gauges from direct exposure to the hypersonic flow. In addition, these gauges face the recirculation conical cavity flow.

The heat transfer rates derived from the platinum gauge output signals shown in Fig. 21 are shown in Fig. 22. For blunt cone body without any spike, a constant heat flux rate is observed during the test time, The results are expressed in terms of Stanton numbers. In the case of the telescopic spiked blunt cone body the peak heat flux rate within the test time, which is consistent for repeated experiments, is considered for the Stanton number calculation. The error in S_t is estimated to be within 8.09% based on the uncertainty analysis of the measurement system.

$$S_t = \frac{q(t)}{\rho_\infty V_\infty (h_0 - h_w)} \tag{3}$$

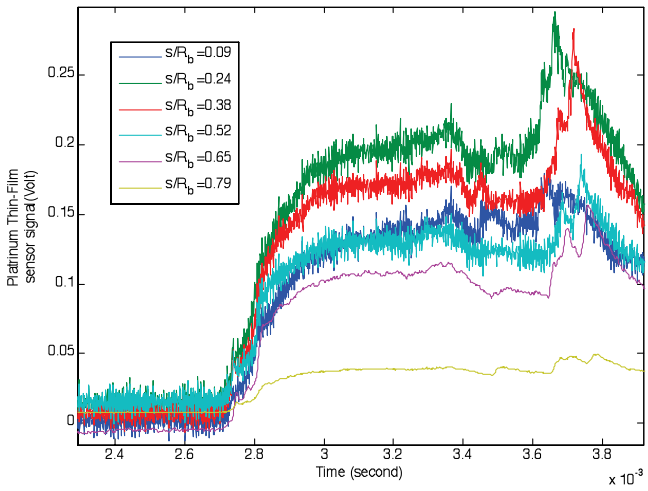

Figure 20. Heat transfer signals for blunt body without spike.

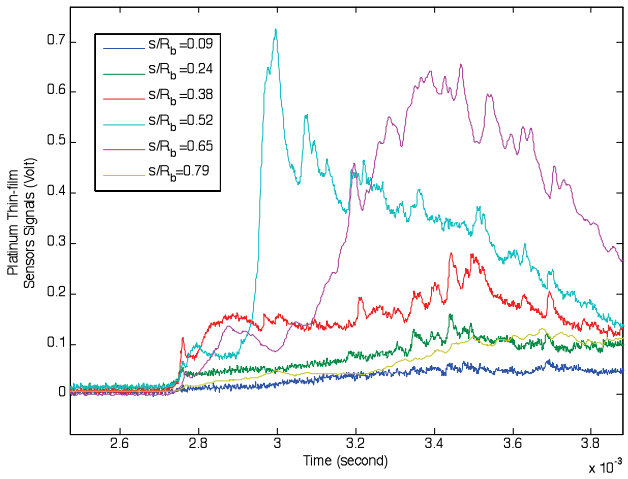

Figure 21. Heat transfer signals for blunt body with telescopic spike.

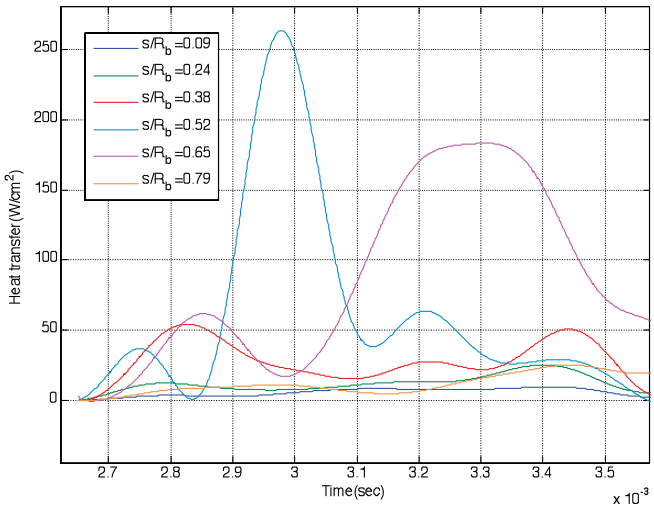

Figure 22 Heat transfer rates corresponding to the signals shown in Fig.21.

The experimental Stanton number variation along one side of the surface at different angles of attack for the blunt cone without any spike is shown in Fig. 23. Similarly, the Stanton number variation for the blunt cone with the conical tipped telescopic aerospike is shown in Fig. 24. It is clearly seen that there is an enhancement of heat transfer rate in the shock interaction region.

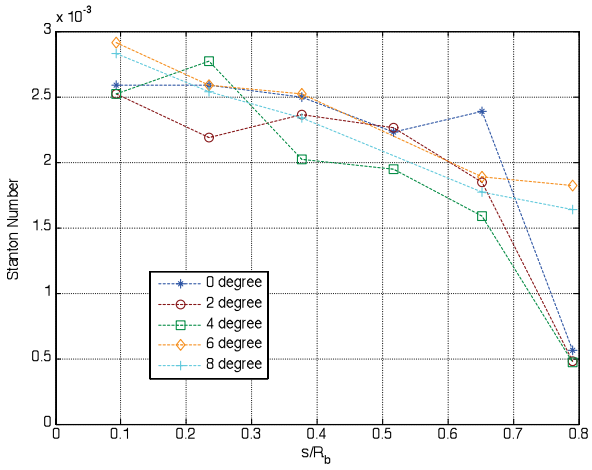

Figure 23. Stanton number variation along the body for conical body without spike at Mach 5.75.

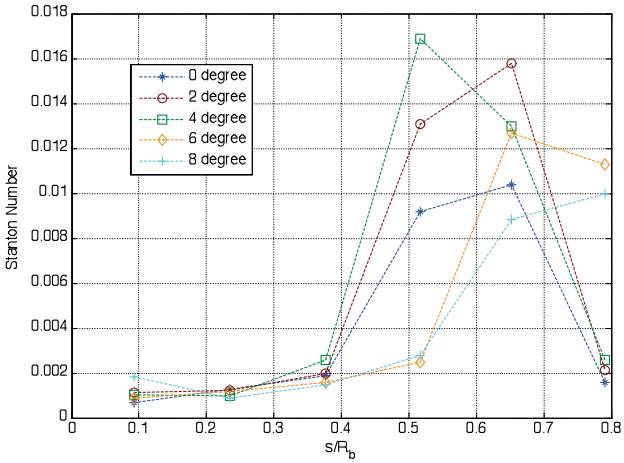

Figure 24. Stanton number variation along the body surface for body with telescopic spike at Mach 5.75.

The second set of experiments was conducted at a Mach number of 7.9 for angles of attack varying from 0 to 10 degree in steps of 2 for all the three cases of blunt cone without aerospike and with plain and telescopic aerospikes. The model was mounted in such a way that the two Macor pieces were kept vertical and therefore the difference in windward and leeward side flow could be identified at angles of attack. The experimental results are presented in terms of Stanton numbers in Figs. 25(a) - (f) for all the three cases at different angles of attack. The negative s/R_b denotes the windward side and the positive value denotes the leeward side of flow over the model. Since in the case of the blunt cone with a spike there is a conical shock which interacts with the reattachment shock over the blunt cone surface, the flow region within this conical shock is a low pressure and low temperature recirculation region. Therefore heat transfer rates measured nearer to the nose of the blunt cone are lower for the case of the blunt cone with an aerospike compared to the blunt cone body without any aerospike. The heat transfer rates increase with increasing s/R_b due to the shock-shock interaction.

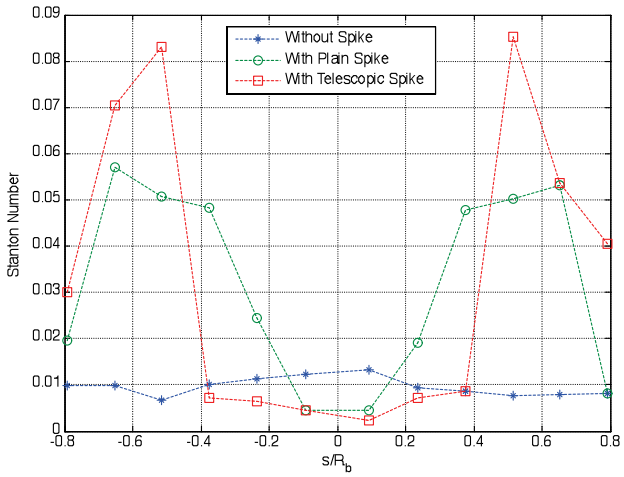

(a) $\alpha = 0^o$

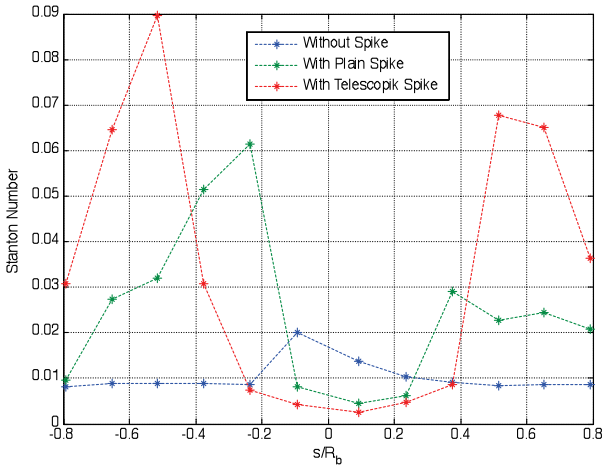

(b) $\alpha = 2^o$

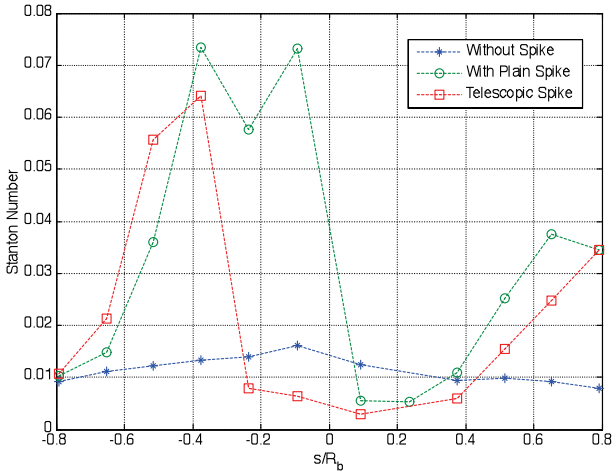

(c) $\alpha = 4^o$

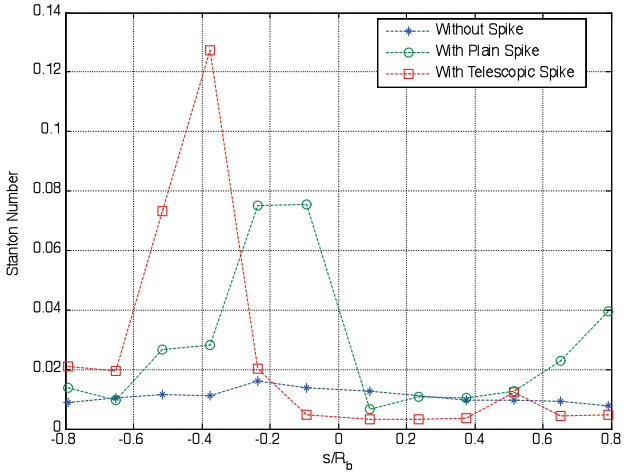

(d) $\alpha = 6^o$

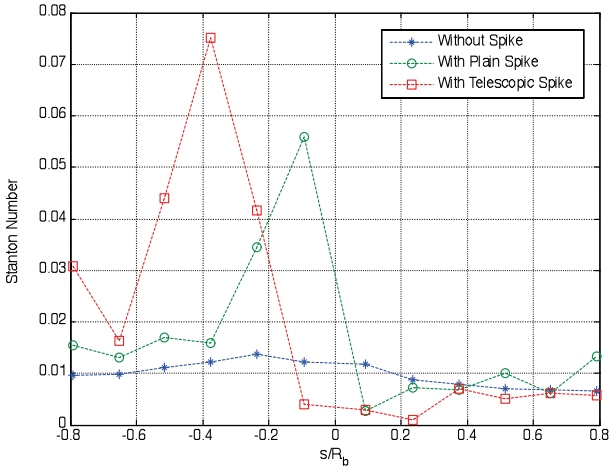

(e) $\alpha = 8^o$

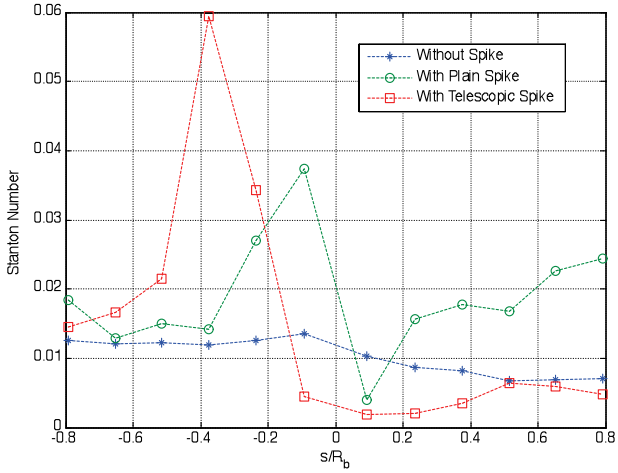

(f) $\alpha = 10^o$

Figure 25 (a)-(f). Heat transfer rates over the blunt cone surface at Mach 7.9 at different angles of attack.

Comparison of measured heat transfer rates for the blunt cone with the conical tipped plain aerospike and the telescopic aerospike leads to the following explanation of the flow physics. In the later case the stabilizer disk sitting in front of the nose of the blunt cone blocks higher energy flow and hence the sensors close to the stagnation point encounter only low energy deep conical cavity flow. Therefore the heat transfer rates further decrease when the blunt cone is attached with the telescopic spike. But the shock interaction in this case is stronger than that with the plain spike. As the angle of attack increases the shock interaction point on the leeward side moves away from the nose, which is evident from the decreasing heat transfer rates. In addition, the rate of decrease of heat transfer rates in the leeward side with respect to the angle of attack is higher for the telescopic spike than for the plain spike. Beyond 2° angle of attack the shock interaction slips out of the blunt cone periphery on the leeward side and hence at higher angles of attack the telescopic spike is more effective in reducing the heat transfer rates compared to the plain spike. On the windward side, the maximum heat transfer rate is observed at 6° angle of attack at the location of the shock interaction.

The measured heat transfer rates for all three cases of the blunt cone without any spike, attached with the conical tipped plain spike and the telescopic spike are consolidated in Figs. 26-28, respectively. It is seen that surface of the blunt cone in absence of any spike in general faces the maximum heat transfer rates nearer to the nose region due to the stagnation of the high energy flow which has been eliminated by the presence of spike.

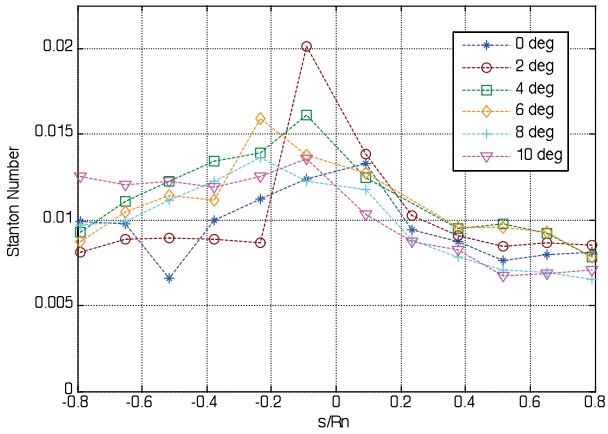

Figure 26. Heat transfer rates for blunt cone without spike at Mach 7.9.

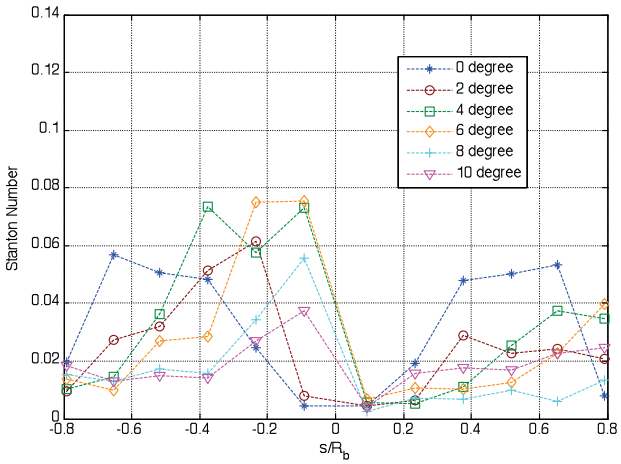

Figure 27. Heat transfer rates for blunt cone with plain spike at Mach 7.9.

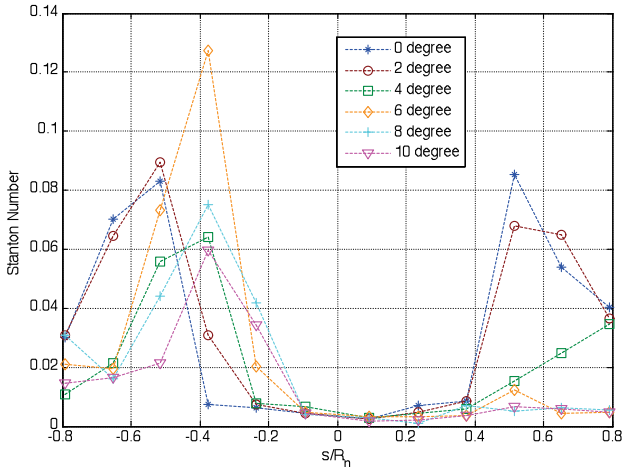

Figure 28. Heat transfer rates for blunt cone with telescopic spike at Mach 7.9.

The shock interaction is unsteady in nature. Therefore, the heat transfer rate increase is for a time less than 100µs. The magnitude of this transient heat transfer rate is very much higher than the value estimated using the Fay and Riddell expression [26], which is found to be 43 W/cm^2 for the flow enthalpy of 2.1MJ/kg. The measured value for the blunt cone without any spike nearer to the stagnation point at s/R_b = 0.092 is 24 W/cm^2. This measured value is less than the theoretically estimated value because of the location of the gauge away from the exact stagnation point.

As discussed above, the shock generated by the conical tip telescopic aerospike interacts with the re-attachment shock of the blunt cone body and the location of the shock interaction can be inferred from the heat transfer data shown in Fig. 24 and Fig. 28. Using this data, it is possible to draw cubic curves which represent the shock-shock interaction profiles at different angles of attack. This profile over the blunt cone in the presence of the telescopic spike is shown in Fig. 29. At zero angle of attack the shock interaction profile is exactly circular in nature and, as the angle of attack increases, the shock interaction approaches towards the nose of the blunt cone until 6º on the windward side. Even if the angle of attack is increased further, the shock interaction cannot come closer beyond a certain limit due to the presence of the discs on the spike. On the leeward side, the shock interaction point moves away from the nose and it prevails within the blunt cone periphery until 4º. Beyond this angle of attack it just slips out of the blunt cone surface. In the sideways the shock interaction profile comes closer toward the nose until the profile slips out of the periphery on the leeward side. When there is no shock interaction on the leeward side, the flow has a rapid expansion. Therefore, it affects the overall profile and the profile expands on the sides.

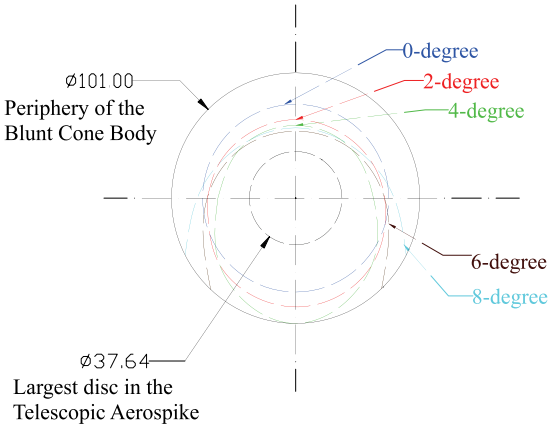

Figure 29. Shock- shock interaction profile.

CONCLUSION

The effects of addition of forward facing aerospikes of different geometries on the aerodynamic parameters of the large angle blunt cone flying at hypersonic Mach numbers of 5.75 and 7.9 was investigated experimentally for different angles of attack. The measurements carried out include measurements of the heat transfer rates and aerodynamic drag along with the visualization of flow patterns using a high speed schlieren technique around the blunt cone without any spike and with a plain and a telescopic spike. It is found that at larger angles of attack the performance of the telescopic aerospike as a drag reduction device is superior to that of the plain aerospike. However, it is found that the inclusion of an aerospike results in creation of high heat transfer rates at certain locations on the model surface due to the interaction of the oblique shock generated by the aerospike with the reattachment shock on the surface of the blunt cone. It is found that this increase in the heat transfer rate is larger for the telescopic aerospike than for the plain aerospike. At angles of attack, the shock interaction moves away from the nose on leeward side and the heat flux rate decreases while the shock interaction moves towards the nose of the blunt cone body on the windward side and the heat flux rate attains a maximum level at a 6^{o} angle of attack. Essentially this study shows that the telescopic aerospike is an effective drag reduction device at higher angles of attack while its role on the heat transfer rates needs to be studied further.

ACKNOWLEDGMENTS

The authors would like to thank all the members in the high enthalpy aerodynamics laboratory for their support to carry out the experiments.

REFERENCES

1. Shang, J. S., Hayes, J., Wurtzler, K., and Strang, W., "Jet-Spike Bifurcation in High-Speed Flows," *AIAA Journal*, Vol. 39, No.6, 2001, pp. 1159-1165. doi: 10.2514/2.1430.
2. Venukumar B, Jagadeesh, G., and Reddy, K.P.J., "Counter Flow Drag Reduction by Supersonic Jet for a Blunt Body in Hypersonic Flow," *Physics of Fluids*, Vol. 18, No.11, 2006, 118104. doi: 10.1063/1.2401623
3. Minucci, M. A. S., Bracken, R. M., Myrabo, L. N., Nagamatsu, H. T., and Shanahan, K. J., "Experimental Investigation of an Electric Arc Simulated Air spike in Hypersonic Flow," 38^{th} Aerospace Sciences Meeting and Exhibit, 10-13 Jan. 2000 / Reno, NV, AIAA-00-0715.
4. Shang, J. S., "Plasma Injection for Hypersonic Blunt-Body Drag Reduction," *AIAA Journal*, Vol. 40, No. 6, 2002, pp. 1178-1185. doi: 10.2514/2.1769
5. Vinayak Kulkarni and Reddy, K. P. J., "Enhancement in Counterflow Drag Reduction by Supersonic Jet in High Enthalpy Flows", *Physics of Fluids*, Vol. 20, No. 1, 2008, 016103. doi: 10.1063/1.2813042
6. Vinayak Kulkarni, Hegde, G. M., Jagadeesh, G., Arunan, E. and Reddy, K. P. J., "Aerodynamic Drag Reduction by Heat Addition into the Shock Layer for a Large Angle Blunt Cone in Hypersonic Flow", *Physics of Fluids*, Vol. 20, No. 8, 2008, 081703. doi: 10.1063/1.2944982
7. Satheesh, K., and Jagadeesh, G., "Experimental Investigations on the Effect of Energy Deposition in Hypersonic Blunt Body Flow Field," *Shock Waves*, Vol. 18, No. 1, 2008, pp.53-70. doi: 10.1007/s00193-008-0140-3
8. Carlos Zorea and Josef Rom, "Effect of a Spike on the Drag and on the Aerodynamic Stability of Blunt Bodies in Supersonic Flow," *Journal of Spacecraft and Rockets*, Vol. 7, No. 8, 1970, pp. 1017-1019. doi: 10.2514/3.30094
9. Viren Menezes, Saravanan S., Jagadeesh G., and Reddy K.P.J., "Experimental Investigations of Hypersonic Flow over Highly Blunted Cones with Aerospikes." *AIAA Journal*, Vol. 41, No. 10, 2003, pp 1955-1966. doi: 10.2514/2.1885
10. Crawford, Davis H., "Investigation of the Flow over a Spiked-Nose Hemisphere-Cylinder at a Mach number of 6.8," NASA TN-D-118, Dec. 1959.

11. Maull, D. J., "Hypersonic Flow over Axially Symmetric Spiked Bodies," *Journal of Fluid Mechanics*, Vol. 8, No.4, 1960, pp. 584-592. doi: 10.1017/S0022112060000815
12. Wood, C. J., "Hypersonic Flow over Spiked Cones," *Journal of Fluid Mechanics*, Vol. 12 No.4, 1962, pp. 614-624. doi: 10.1017/S0022112062000427
13. Guenther R. A and Peter Reding, J., "Fluctuating Pressure Environment of a Drag Reduction Spike," *Journal of Spacecraft and Rockets*, Vol.14, No.12, 1977, pp. 705-710. doi: 10.2514/3.57253
14. Kobayashi H, Maru H, Hongoh M, Takeuchi S, Okai K and Kojima T, "Study on variable-shape supersonic inlets and missiles with MRD device", Acta Astronautica, Vol. 61, No. 11-12, Dec. 2007, pp. 978-988, doi: 10.1016/j.actaastro.2006.12.018.
15. Truitt R.W., "Hypersonic Aerodynamics," The Ronald Press Company, 1959.
16. Tillmann W., "Additional Measurements of the Drag of Surface Irregularities in Turbulent Boundary Layers," NACA Technical Memorandum 1299, January 1951.
17. Zaugol'nikov N. L., Koval M. A., and Shvets A. I., "Fluctuation in Cavities in a Supersonic Gas Flow," Fluid Dynamics, Vol.25, No.2, 1990, pp. 266-272. doi: 10.1007/BF01058979
18. Anatol Roshko, "Some Measurements of Flow in a Rectangular Cutout," NACA Technical Note 3488, August 1955.
19. Rossitor J. E., "Wind-Tunnel Experiments on the Flow over Rectangular Cavities at Subsonic and Transonic Speeds," Aeronautical Research Council Reports and Memoranda No. 3438, October 1964.
20. Gharib M and Roshko A., "The Effect of Flow Oscillations on Cavity Drag," Journal of Fluid Mechanics, Vol.177, 1987, pp.501-530. doi: 10.1017/S002211208700106X.
21. Niranjan Sahoo and Reddy, K. P. J., "Force Measurement Techniques for Hypersonic Flows in Shock Tunnels," International Journal of Hypersonics, Vol. 1, No.1, 2010, pp. 31-57.
22. Vidal, R. J., "Model Instrumentation Techniques for Heat Transfer and Force Measurements in a Hypersonic Shock Tunnel," Cornell Aeronautical Laboratory Report WADC TN 56-315, 1956.
23. Satheesh, K., and Jagadeesh, G., "Analysis of an internally mountable accelerometer balance system for use with non-isotropic models in shock tunnels," Measurement, Vol. 42, No. 6, 2009, pp. 856-862, doi: 10.1016/j.measurement.2009.01.010.
24. Remy Prost and Robert Goutte, "Discrete Constrained Iterative Deconvolution Algorithms with Optimized Rate of Convergence," Signal Processing, Vol. 7, No.3, 1984, pp. 209-230. doi: 10.1016/0165-1684(84)90001-X.
25. Cook, W. J., and Felderman, E. J., "Reduction of Data from Thin Film Heat Transfer Gauges: A Concise Numerical Technique," AIAA Journal, Vol. 4, No.3, 1966, pp. 561-562. doi: 10.2514/3.3486.
26. Fay, J. A., and Riddell, F. R., "Theory of Stagnation Point Heat Transfer in Dissociated Air," Journal of the Aeronautical Sciences, Vol. 25, No.2, 1958, pp. 73-85.